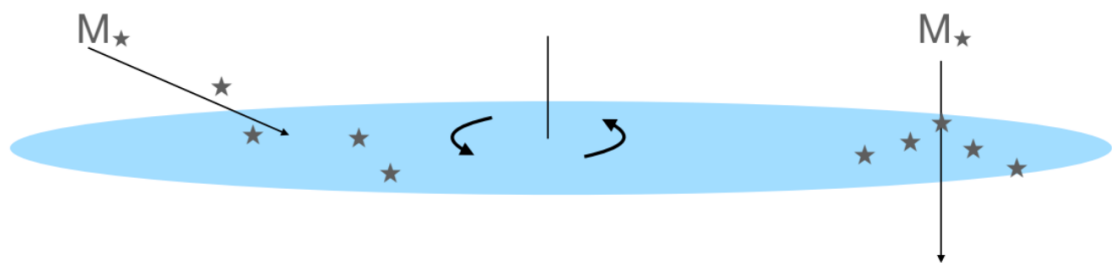


Numerical Methods Project:

Galactic Disc Heating

The response of the stellar component
to an external perturbation



Written by:
Annus Haider & Anna Schann

Supervised by Christian Boily

Academic year 2025-2026

Contents

Introduction	3
1 Physical model	4
1.1 Gravitational potential	4
1.2 Equations of motion	4
1.3 Realistic disc initialization	5
2 Numerical methods	7
2.1 ODE formulation and state vector	7
2.2 Leapfrog integrator	7
2.3 Runge-Kutta 4 integrator	8
2.4 Time-step selection	9
2.5 Conservation diagnostics (Energy & Angular Momentum)	9
3 Numerical validation	11
3.1 Purpose	11
3.2 Orbits in the unperturbed disc	11
3.3 Energy conservation: Leapfrog vs RK4	12
3.4 Stability of the disc	13
4 Results	15
4.1 Description of the external perturbation	15
4.2 Response to external perturbations	16
4.3 Inclined Perturber	19
5 Perspectives on parallelization	22
5.1 Parallelization strategy	22
5.2 Possible implementations	22
5.3 Benefits and limitations	22
Conclusion	23
References	24

List of Figures

1	Representative orbits for a single star in the Milky Way disc. The left panel shows the face-on view ($x-y$), while the right panel shows the edge-on view ($R-z$)	11
2	Orbits of three stars in the Milky Way disc. The left panel shows the face-on view ($x-y$), while the right panel shows the edge-on view ($z-x$).	12
3	The left panel shows energy conservation with bounded periodic drifts, while the right panel shows relative energy change with respect to the angular momentum of each star	12
4	The left panel shows a secular energy drift over long integration times, while the right panel shows relative energy change with respect to the angular momentum of each star	13
5	Angular momentum L_z of all stars vs. time.	13
6	The left panel shows global velocity dispersion with time, while the right panel shows Schwarzschild velocity distribution.	14
7	The left panel shows v_R with time, while the right panel shows the time variation of v_z	14
8	Orthogonal and Inclined trajectory of the perturber.	15
9	Orthogonal trajectory of the perturber.	16
10	The left panel shows the energy conservation, while the right panel shows the physical energy injection and redistribution.	17
11	Relative energy change with respect to angular momentum.	17
12	The left panels shows evolution of σ_R while the right shows the evolution of σ_Z	18
13	The left panels shows the structure of disk after perturbation while the right shows the number of stars ejected from the disk plane.	18
14	Trajectory of inclined perturber.	19
15	Energy change vs energy injection.	19
16	Energy change with respect to angular momentum.	20
17	Evolution of velocity dispersion profiles.	20
18	Disk structure and number of unboud stars.	21

Introduction

A galactic disc is a fundamental component of a galaxy. Observations show that it is commonly described as consisting of a thin stellar component and a vertically extended thick disc. These properties indicate that galactic discs are not dynamically cold systems, and suggest the action of various heating processes responsible for the observed kinematic substructures.

Classical internal mechanisms alone cannot fully explain the observed amplitude of these properties. Interactions with external perturbations, such as the passage of satellite galaxies, massive clumps, or other compact objects through or near the disc plane, are therefore expected to play a key role in the dynamical evolution of galactic discs. Studying how such perturbations transfer energy and angular momentum to stars is essential to understand the present-day structure and kinematics of galactic discs.

The aim of this numerical project is to study the dynamical heating of a stellar disc induced by the passage of an external perturbing object. We model the disc as a collisionless stellar system evolving in a fixed gravitational potential, in order to isolate the response of stellar orbits to an external disturbance. The gravitational potential of the disc is described by the analytic Miyamoto-Nagai potential, which provides a simple but realistic representation of a flattened galactic disc.

From a numerical point of view, we integrate the orbits of individual stars over several dynamical timescales. The stellar trajectories are computed in cylindrical coordinates using time integration schemes adapted to hamiltonian systems. We compare a symplectic leapfrog integrator with a fourth-order Runge–Kutta method, and evaluate their accuracy and stability through tests of energy conservation and the long-term evolution of an unperturbed disc.

The initial conditions of the stellar population are drawn from a realistic phase-space distribution, consistent with the chosen potential and with observationally motivated velocity dispersions. By integrating a large number of stellar orbits simultaneously, we obtain a statistical description of the disc response to the perturbation. The resulting disc heating is quantified through the evolution of radial and vertical velocity dispersions, as well as changes in the orbital energy of the stars. By varying the properties of the perturber, such as its mass and trajectory, we explore how different types of perturbers affect the efficiency and spatial distribution of disc heating.

This work therefore combines a physically motivated galactic model with a careful numerical approach, providing insight into the mechanisms by which external perturbations contribute to the dynamical evolution of stellar discs.

1 Physical model

1.1 Gravitational potential

In this work, we modeled the gravitational field of the galactic disc using the analytic Miyamoto–Nagai potential. This potential provides a simple but realistic description of a flattened stellar disc, while allowing for fast and accurate force evaluations, which is essential for orbit integration involving a large number of particles.

The Miyamoto-Nagai potential is given by

$$\Phi(R, z) = -\frac{GM}{\sqrt{R^2 + (a + \sqrt{z^2 + b^2})^2}} \quad (1)$$

where (R, ϕ, z) are the cylindrical coordinates, M is the total mass of the disc, and a and b are scale parameters controlling the radial and vertical extent of the mass distribution. The parameter a sets the disc scale length, while b determines its vertical thickness. [1]

This potential belongs to a class of analytic potential-density pairs, meaning that it corresponds to a well-defined mass density distribution that satisfies the Poisson's equation. As a result, it provides a self-consistent gravitational background for the stellar disc, without requiring the explicit computation of the disc self-gravity during the orbit integration. The Miyamoto-Nagai potential is widely used in galactic dynamics studies because it captures the main geometric properties of disc galaxies while remaining computationally efficient. In the context of this project, it allows us to focus on the dynamical response of stellar orbits to an external perturbation, without introducing unnecessary numerical complexity.

The values of the parameters M , a , and b are chosen to roughly reproduce the mass distribution and scale lengths of the Milky Way disc. This choice ensures that the characteristic orbital timescales and velocity scales are representative of a realistic galactic environment, while remaining within a simplified and controlled modeling framework.

1.2 Equations of motion

The motion of stars in the galactic disc is described within an Hamiltonian framework. Since the disc is modeled as a collisionless system evolving in a fixed gravitational potential, each star follows an independent orbit governed by the gravitational field of the disc and, when present, by an external perturbation.

We work in cylindrical coordinates (R, ϕ, z) , which are well suited to the axisymmetric geometry of the disc. In the absence of an external perturber, the system is axisymmetric and time-independent, implying the conservation of the angular momentum around the symmetry axis,

$$L_z = Rv_\phi, \quad (2)$$

as well as the conservation of the total orbital energy

$$E = \frac{1}{2} (v_R^2 + v_\phi^2 + v_z^2) + \Phi(R, z). \quad (3)$$

Using these coordinates, the equations of motion for a star in the Miyamoto–Nagai potential can be written as

$$\frac{dR}{dt} = v_R, \quad (4)$$

$$\frac{dz}{dt} = v_z, \quad (5)$$

$$\frac{d\phi}{dt} = v_\phi = \frac{L_z}{R^2}, \quad (6)$$

$$\frac{dv_R}{dt} = \frac{L_z^2}{R^3} + F_R(R, z), \quad (7)$$

$$\frac{dv_z}{dt} = F_z(R, z), \quad (8)$$

where $F_R = -\partial\Phi/\partial R$ and $F_z = -\partial\Phi/\partial z$ are the radial and vertical components of the gravitational force derived from the potential.

This formulation highlights the separation between the azimuthal motion, which is fully determined by the conserved angular momentum in the unperturbed case, and the radial and vertical motions, which are directly driven by the gravitational forces. It also provides a convenient framework for numerical integration, as the system reduces to a set of first-order ordinary differential equations.

When an external perturber is introduced, the axisymmetry of the system is broken and neither the energy nor the angular momentum of individual stars is conserved. Deviations from these conserved quantities therefore provide a direct measure of the dynamical impact of the perturbation and will be used later to quantify disc heating.

1.3 Realistic disc initialization

In order to study the dynamical response of the stellar disc to an external perturbation, it is essential to construct initial conditions that are both physically motivated and numerically stable. The stellar disc is therefore initialized using a realistic spatial and kinematic distribution, consistent with the chosen gravitational potential.

1.3.1 Spatial structure

The radial distribution of stars is modeled as an exponential disc,

$$\Sigma(R) \propto \exp\left(-\frac{R}{R_d}\right), \quad (9)$$

where R_d is the radial scale length of the disc. In the vertical direction, the stellar distribution is taken to be Gaussian,

$$\rho(z) \propto \exp\left(-\frac{z^2}{2h^2}\right), \quad (10)$$

with h the vertical scale height. This choice provides a simple but realistic description of a thin stellar disc, while remaining straightforward to sample numerically.

1.3.2 Velocity distribution function

The velocity field of the stellar disc is initialized using a Schwarzschild distribution function, which is commonly adopted to describe collisionless stellar systems in approximate dynamical equilibrium. In this framework, the velocity components are assumed to follow Gaussian distributions around the local mean motion.

Within the epicyclic approximation, the radial and azimuthal velocity dispersions are related by

$$\sigma_\phi(R) = \frac{\kappa(R)}{2\Omega(R)} \sigma_R(R), \quad (11)$$

where $\Omega(R)$ is the circular angular frequency and $\kappa(R)$ is the epicyclic frequency derived from the gravitational potential. This relation is used to compute the azimuthal velocity dispersion self-consistently from the prescribed radial dispersion. [2]

The radial and vertical velocity dispersions, $\sigma_R(R)$ and $\sigma_z(R)$, are prescribed as decreasing functions of radius, motivated by observations of galactic discs. The radial and vertical velocities of individual stars are then drawn from Gaussian distributions with these dispersions.

The azimuthal velocity of each star is sampled around the local circular velocity $v_c(R)$, with a dispersion $\sigma_\phi(R)$ computed from the epicyclic approximation. This prescription provides a realistic velocity field that remains close to centrifugal equilibrium in the unperturbed case.

1.3.3 Validation of the initial disc

The validity of the initial conditions is assessed through a series of numerical checks performed in the absence of any external perturbation. Orbit maps in face-on and edge-on projections are used to verify the expected epicyclic motion of stars in the disc. In addition, the input velocity dispersions are recovered after several orbital periods, demonstrating that the disc is in approximate equilibrium.

Finally, the long-term stability of the radial and vertical velocity dispersions is verified, confirming that no artificial heating is introduced by the initial conditions or by the numerical integration scheme in the unperturbed case. These tests ensure that any subsequent evolution of the disc can be confidently attributed to the presence of an external perturbation.

2 Numerical methods

In this section, we describe the numerical methods used to integrate stellar orbits in a fixed galactic potential. The equations of motion are solved using time-integration schemes adapted to Hamiltonian systems, with an emphasis on accuracy and conservation properties. We present the formulation of the equations, the numerical integrators employed, and the criteria used to assess their performance.

2.1 ODE formulation and state vector

The stellar disc is modeled as a collisionless system evolving in a fixed, axisymmetric gravitational potential. Individual stellar trajectories are integrated by solving the equations of motion in cylindrical coordinates (R, ϕ, z) , which are well suited for disc geometries. In the absence of non-axisymmetric perturbations, the vertical component of the angular momentum L_z is conserved and treated as a constant parameter for each orbit.

The phase-space evolution of a star is described by the state vector

$$\mathbf{y} = (R, z, \phi, v_R, v_z), \quad (12)$$

where v_R and v_z denote the radial and vertical velocity components, respectively. The azimuthal velocity is obtained from angular momentum conservation as

$$v_\phi = \frac{L_z}{R}. \quad (13)$$

The equations of motion are written as a system of first-order ordinary differential equations,

$$\frac{d\mathbf{y}}{dt} = \mathbf{f}(\mathbf{y}, t), \quad (14)$$

with the radial and vertical accelerations given by

$$\ddot{R} = \frac{L_z^2}{R^3} - \frac{\partial \Phi}{\partial R}, \quad (15)$$

$$\ddot{z} = -\frac{\partial \Phi}{\partial z}, \quad (16)$$

where $\Phi(R, z)$ denotes the gravitational potential of the host galaxy, which in this work is modeled by a Miyamoto–Nagai potential representing the thin disk of the Milky Way. The first term in the radial equation corresponds to the centrifugal acceleration arising from angular momentum conservation.

When an external perturber is present, its gravitational contribution is added to the host potential, and the total forces are evaluated consistently at each timestep. The perturber is treated as a softened point mass moving along a prescribed trajectory, resulting in a time-dependent, non-axisymmetric perturbation.

All equations of motion are integrated in a fully vectorized manner, allowing the simultaneous evolution of several hundred stellar orbits. This approach ensures computational efficiency and enables a statistical description of the disc response to external perturbations.

2.2 Leapfrog integrator

The primary numerical scheme used to integrate the equations of motion is a second-order Leapfrog integrator, implemented in a kick–drift–kick formulation. This explicit time-integration method is particularly well suited for Hamiltonian systems, such as collisionless stellar dynamics, due to its symplectic nature.

At each timestep, the velocities are first advanced by half a timestep using the accelerations evaluated at the current positions. The positions are then updated over a full timestep using the intermediate velocities, after which the velocities are completed by a second half-step kick using the newly computed accelerations. This staggered update ensures second-order accuracy in time while preserving the phase-space structure of the system. In an axisymmetric potential, the Leapfrog scheme conserves the vertical component of the angular momentum L_z exactly by construction. Since the azimuthal motion is evolved using the relation $v_\phi = L_z/R$, no numerical torques are introduced in the absence of non-axisymmetric forces.

A key advantage of the Leapfrog integrator is its long-term stability. Although the total energy is not conserved exactly at each timestep, the symplectic nature of the scheme guarantees that the relative energy error remains bounded and oscillatory over time, rather than exhibiting a secular drift. This behaviour makes the Leapfrog method particularly suitable for long-term integrations of stellar orbits, where accurate conservation properties are essential for distinguishing physical heating from numerical artefacts.

2.3 Runge-Kutta 4 integrator

In order to compare different numerical integration schemes, we also implemented a fourth-order Runge-Kutta integrator (RK4). This method advances the system by combining several intermediate evaluations of the equations of motion within a single timestep, leading to fourth-order accuracy in time.

The equations of motion are written in the form

$$\frac{d\mathbf{y}}{dt} = \mathbf{f}(\mathbf{y}), \quad (17)$$

where $\mathbf{y} = (R, z, \phi, v_R, v_z)$ is the phase-space state vector. Starting from \mathbf{y}_n at time t_n , the RK4 scheme computes four intermediate slopes,

$$\mathbf{k}_1 = \mathbf{f}(\mathbf{y}_n), \quad (18)$$

$$\mathbf{k}_2 = \mathbf{f}\left(\mathbf{y}_n + \frac{\Delta t}{2} \mathbf{k}_1\right), \quad (19)$$

$$\mathbf{k}_3 = \mathbf{f}\left(\mathbf{y}_n + \frac{\Delta t}{2} \mathbf{k}_2\right), \quad (20)$$

$$\mathbf{k}_4 = \mathbf{f}(\mathbf{y}_n + \Delta t \mathbf{k}_3), \quad (21)$$

which are then combined to update the solution,

$$\mathbf{y}_{n+1} = \mathbf{y}_n + \frac{\Delta t}{6} (\mathbf{k}_1 + 2\mathbf{k}_2 + 2\mathbf{k}_3 + \mathbf{k}_4). \quad (22)$$

This procedure provides high accuracy for individual timesteps and allows orbital trajectories to be resolved with good precision over short integration times. However, the RK4 scheme is not symplectic, and therefore does not preserve conserved quantities such as the total energy exactly. Over long integration times, this may lead to a slow secular drift in energy.

For this reason, the RK4 integrator is mainly used here as a comparison tool. Its energy conservation properties are contrasted with those of the symplectic leapfrog scheme in order to assess the impact of the numerical method on long-term orbital integrations.

2.4 Time-step selection

The stellar disk is evolved using a symplectic leapfrog integrator with a fixed time-step Δt chosen to resolve stellar orbits accurately. The key parameters for the simulation are:

- Number of stars: $N_{\text{stars}} = 500$
- Time-step: $\Delta t = 1 \times 10^{12} \text{ s} \approx 0.0317 \text{ Myr}$
- Total number of steps: $n_{\text{steps}} = 20,000$

The total physical duration of the simulation is therefore

$$t_{\text{total}} = n_{\text{steps}} \times \Delta t \approx 20,000 \times 0.0317 \text{ Myr} \approx 634 \text{ Myr}.$$

This corresponds to approximately three full revolutions of a Sun-like star at $R \sim 8 \text{ kpc}$, given that the orbital period is $T_{\text{orb}} \sim 220 \text{ Myr}$.

Each integration step advances a star by a fraction of an orbit

$$f_{\text{orbit/step}} = \frac{\Delta t}{T_{\text{orb}}} \approx \frac{0.0317}{220} \approx 1.44 \times 10^{-4},$$

which corresponds to an angular motion of

$$\Delta\theta_{\text{step}} = 360^\circ \times f_{\text{orbit/step}} \approx 0.05^\circ$$

along its orbit. This small fraction ensures that the leapfrog integrator accurately resolves orbital motion while conserving angular momentum exactly and maintaining bounded energy errors over the full duration.

Thus, the chosen Δt provides a good balance between numerical accuracy and computational efficiency for simulating disk-perturber interactions over multiple orbital periods.

2.5 Conservation diagnostics (Energy & Angular Momentum)

Conservation of energy and angular momentum provides a stringent test of the numerical accuracy of orbit integrations in collisionless systems. In this work, these conserved quantities are used as diagnostic tools to validate the numerical schemes, rather than as physical observables.

In the unperturbed, axisymmetric potential, the vertical component of the angular momentum L_z is conserved exactly by construction, as it is treated as a constant parameter of the equations of motion. Any deviation from constant L_z would therefore indicate numerical or implementation errors.

The total specific energy of each star is given by

$$E = \frac{1}{2} (v_R^2 + v_z^2 + v_\phi^2) + \Phi(R, z), \quad (23)$$

and is monitored throughout the integration. For the Leapfrog integrator, the relative energy error,

$$\frac{\Delta E}{E_0} = \frac{E(t) - E_0}{E_0}, \quad (24)$$

is expected to remain bounded and oscillatory over time, reflecting the symplectic nature of the scheme.

For comparison, integrations performed using a fourth-order Runge–Kutta method exhibit a secular drift in energy, despite their higher local accuracy. This behavior highlights the importance of symplectic integration schemes for long-term simulations of Hamiltonian systems.

All conservation properties discussed here are quantitatively verified in Section 3, where unperturbed orbits are used to demonstrate the numerical stability and reliability of the adopted integration scheme.

3 Numerical validation

3.1 Purpose

The goal of this section is to validate that the orbital integration and thin disc setup reproduce physically reasonable behavior in the absence of external perturbations.

3.2 Orbits in the unperturbed disc

Single star: To highlight epicyclic motion and quasi-periodicity, we first show the circular orbit of a single star initially placed at $R = 8.2$ kpc in the galactic plane.

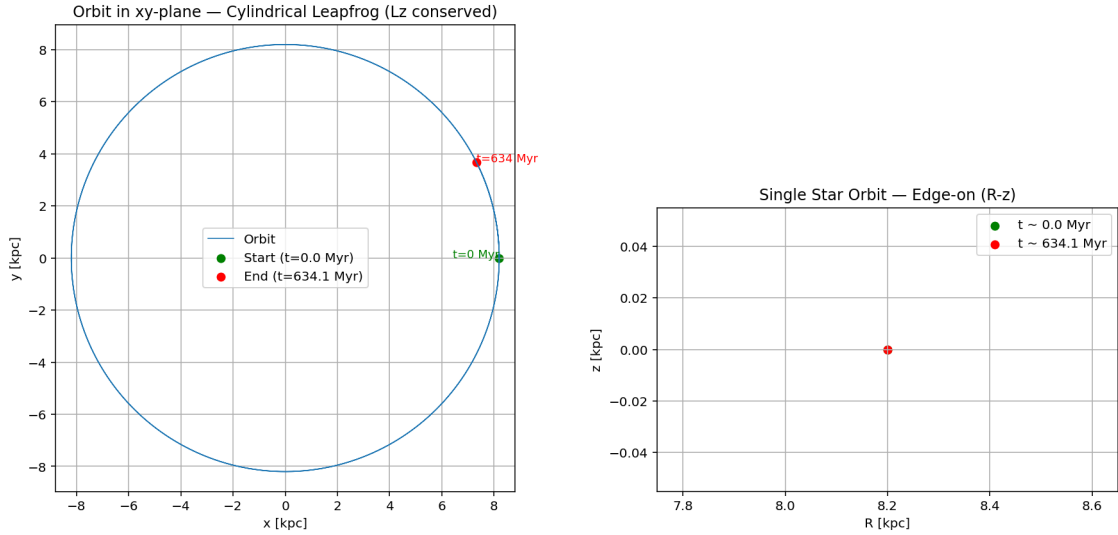


Figure 1: Representative orbits for a single star in the Milky Way disc. The left panel shows the face-on view (x - y), while the right panel shows the edge-on view (R - z).

The star's angular momentum L_z is exactly conserved, and the energy drift remains negligible ($\Delta E / |E_0| \lesssim 10^{-7}$), confirming the numerical stability of the Leapfrog integrator.

Multiple stars: To illustrate typical behavior across the disc, we plot the orbits of three representative stars below. These orbits clearly show quasi-periodic motion and small vertical oscillations, characteristic of a thin disc. A small subsample of stars is used to reduce visual clutter while capturing the diversity of orbital properties and epicyclic frequencies.

All stars conserve L_z exactly, and the maximum relative energy drift remains below 3×10^{-6} . The initial conditions (R , z , v_R , v_z , v_ϕ) produce realistic epicyclic frequencies, confirming that the integration scheme correctly reproduces thin disc dynamics.

3.2.1 Summary

The combination of the "single circular orbit" and the "three epicyclic orbits", along with angular momentum and energy checks, validates the orbital integration. These results provide a robust baseline before setting up entire thin disk and subsequently introducing any external perturbations.

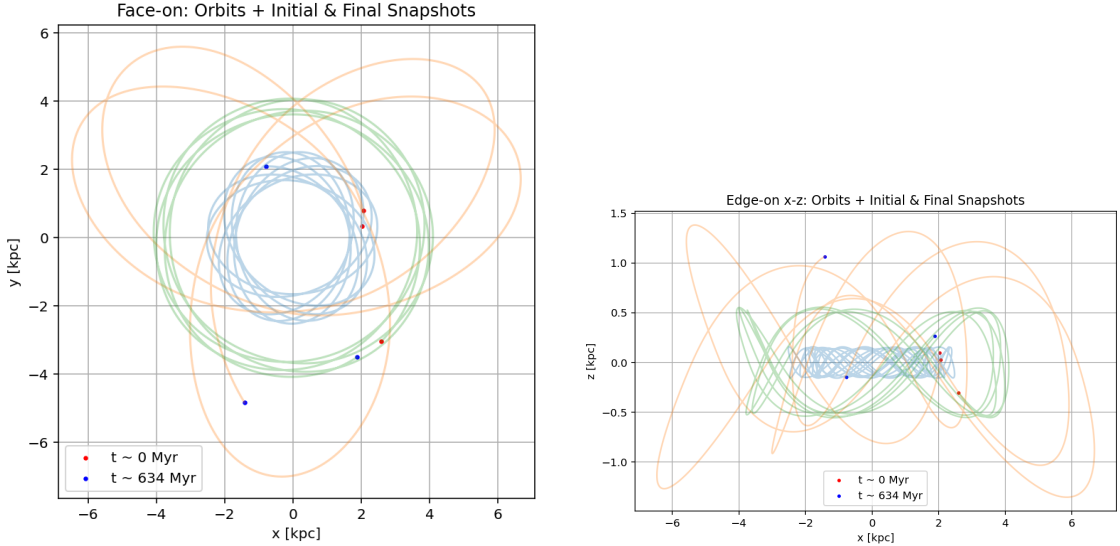


Figure 2: Orbits of three stars in the Milky Way disc. The left panel shows the face-on view (x - y), while the right panel shows the edge-on view (z - x).

3.3 Energy conservation: Leapfrog vs RK4

We tested the long-term conservation of energy and angular momentum in our simulated thin disk using the Leapfrog integrator. Figure 3 shows the relative energy change $\Delta E / |E_0|$ as a function of time for all stars. To summarize the evolution across the ensemble, we also plotted the maximum, minimum, and median values at each timestep, providing a clear picture of the overall energy drift during the simulation. The energy drift remains small throughout the integration, indicating the Leapfrog scheme's excellent symplectic properties.

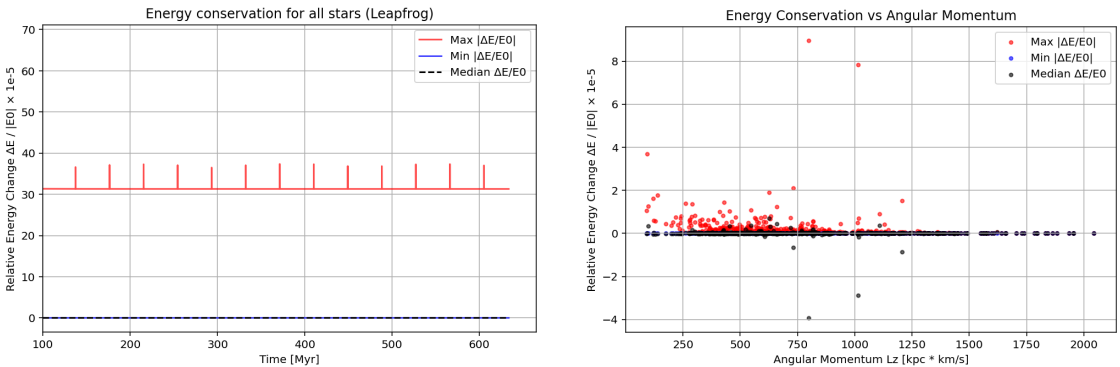


Figure 3: The left panel shows energy conservation with bounded periodic drifts, while the right panel shows relative energy change with respect to the angular momentum of each star

Whereas, the right panel shows the relative energy change as a function of angular momentum L_z , demonstrating that energy conservation is similarly robust across stars with different angular momenta.

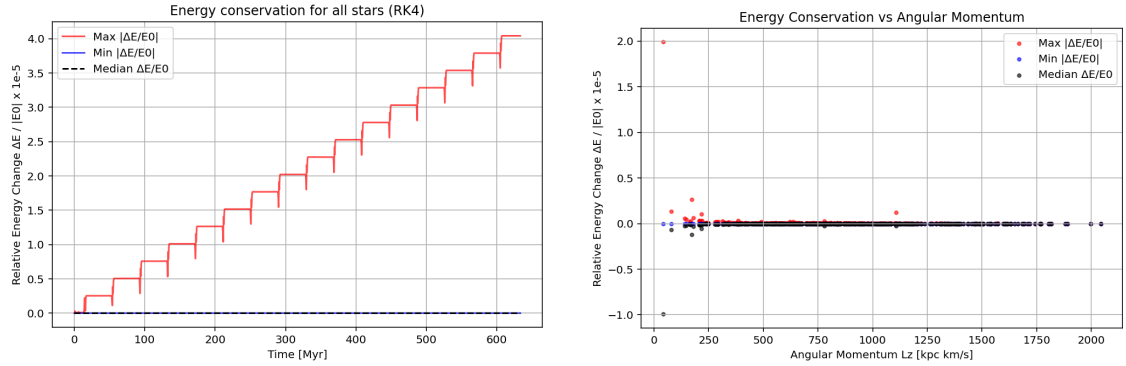


Figure 4: The left panel shows a secular energy drift over long integration times, while the right panel shows relative energy change with respect to the angular momentum of each star

Although the instantaneous energy errors obtained with RK4 remain small, the left panel of Figure 4 clearly shows the presence of a systematic energy drift over time. This behaviour contrasts with the bounded, oscillatory energy variations observed for the Leapfrog integrator. As a consequence, RK4 is less suitable for long-term integrations of Hamiltonian systems, where artificial energy drift can be misinterpreted as physical heating.

Finally, Figure 5 presents the angular momentum L_z of all stars as a function of time. The near-constant values for individual stars confirm that angular momentum is conserved to high precision, as expected in an axisymmetric potential with a symplectic integrator. Together, these results provide confidence in the numerical accuracy and stability of our orbital integration.

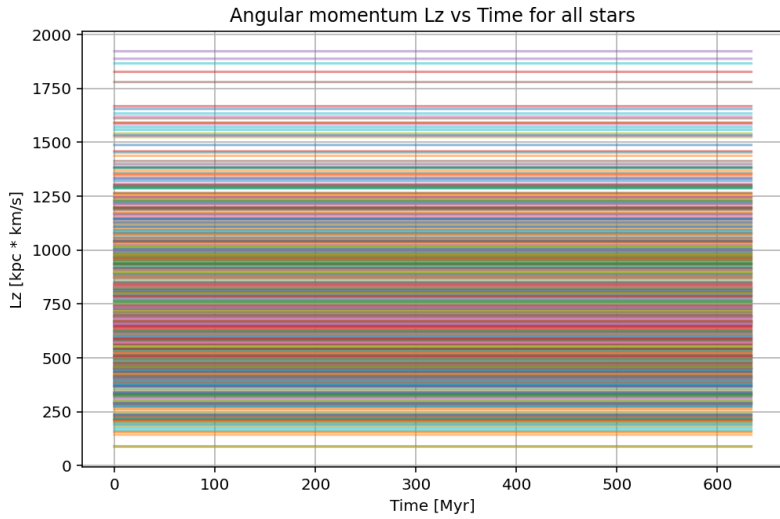


Figure 5: Angular momentum L_z of all stars vs. time.

3.4 Stability of the disc

In this section, we demonstrate the stability of the stellar disc through kinematical diagnostics.

3.4.1 Velocity dispersion and Schwarzschild velocity distribution

The left panel shows the global velocity dispersions of the stellar disc. The radial, azimuthal, and vertical velocity components fluctuate around constant mean values throughout the simulation.

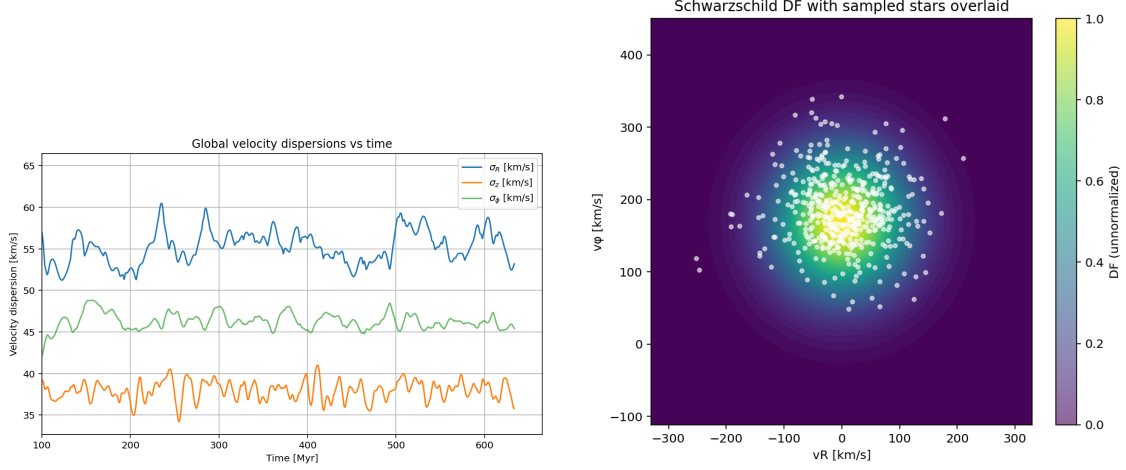


Figure 6: The left panel shows global velocity dispersion with time, while the right panel shows Schwarzschild velocity distribution.

The approximated values are $\sigma_R \approx 55 \text{ km s}^{-1}$, $\sigma_\phi \approx 46.5 \text{ km s}^{-1}$, and $\sigma_z \approx 37.5 \text{ km s}^{-1}$. No systematic increase in these quantities is observed, indicating the absence of numerical heating in the disc. However, the right panel presents the Schwarzschild velocity distribution in the v_R - v_ϕ plane. The distribution exhibits a smooth, elliptical structure, with the highest concentration of stars located near $v_R = 0$ and $v_\phi \simeq 200 \text{ km s}^{-1}$, corresponding to nearly circular stellar orbits. The gradual decrease in phase-space density away from the centre and the lack of asymmetries or high-velocity tails confirm that the disc remains in kinematic equilibrium.

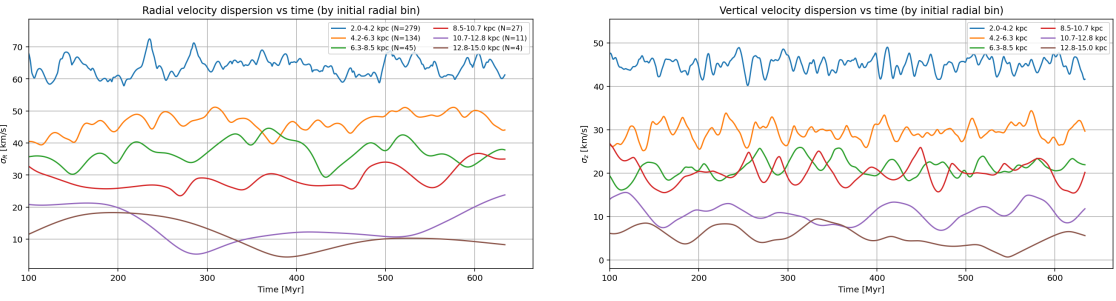


Figure 7: The left panel shows v_R with time, while the right panel shows the time variation of v_z .

Furthermore, Figure 7 clearly illustrates that both v_R and v_z fluctuate around constant mean values, with higher velocities near the galactic center that decrease systematically with increasing

4 Results

4.1 Description of the external perturbation

To study the effect of external encounters on the galactic thin disk, we introduce a single massive perturber modeled as a softened point mass. Its mass ($M_p = 10^{10} M_\odot$) and trajectory is chosen to resemble a realistic satellite galaxy, comparable to the Large Magellanic Cloud (LMC). Such a perturber provides a physically motivated scenario to investigate disk heating and orbital perturbations during close passages. We analyze two types of encounters:

- 1. Orthogonal passage:** The perturber moves along the z -axis, perpendicular to the disk plane, with a straight-line ballistic trajectory. Its impact occurs at a radial distance of $R_{\text{imp}} = 3$ kpc, starting from $z_0 = 50$ kpc with a velocity magnitude $v = 200$ km/s directed toward the disk midplane. This setup isolates the vertical heating effect of a direct perpendicular crossing. Figure 8 gives better visual understanding of the two cases under study.

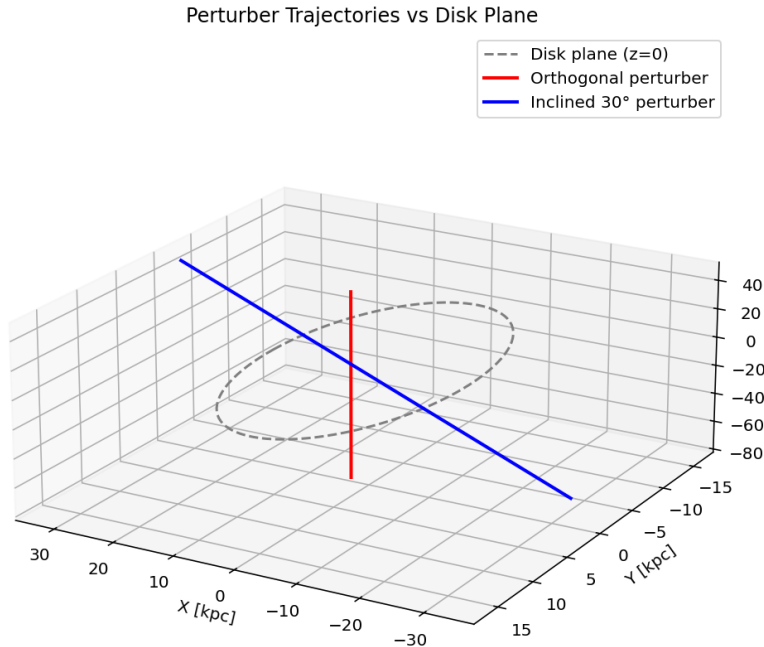


Figure 8: Orthogonal and Inclined trajectory of the perturber.

- 2. Inclined passage:** The perturber crosses the disk at an inclination of 30° relative to the midplane. The initial position and velocity are chosen such that it reaches the same impact radius $R_{\text{imp}} = 3$ kpc. The in-plane and vertical components of the velocity are computed from the inclination, ensuring a straight-line, ballistic motion. This scenario allows us to study combined vertical and radial perturbations on disk stars.

Numerically, the perturber's gravitational force on disk stars is included in the cylindrical leapfrog integrator at each timestep. The total force is the sum of the Miyamoto–Nagai host

potential and the perturber's softened point-mass contribution. The perturber's position is updated as

$$\mathbf{r}_p(t) = \mathbf{r}_0 + \mathbf{v}_0 t,$$

with \mathbf{r}_0 and \mathbf{v}_0 determined by the chosen encounter type. The softening ϵ prevents unphysically large accelerations during close passages. For both cases, the disk evolution is followed for 634 Myr with a timestep of ~ 0.0317 Myr, sufficient to resolve the orbital response of stars while maintaining energy conservation.

By comparing the orthogonal and inclined encounters, we quantify the dependence of disk heating on the orientation of the perturber's passage and its induced changes in velocity dispersions, orbital structure, and energy distribution of the disk stars.

4.2 Response to external perturbations

4.2.1 Orthogonal perturber

4.2.2 Overview and physical setup

We first examine the response of a stellar disk to an orthogonal perturber passing through the disk plane at a galactocentric radius of 3 kpc. The perturber moves perpendicular to the disk at $z = 50$ kpc with a constant velocity = 200 km/s, producing a short-lived but strong tidal interaction. We have analyzed the disk's dynamical response in terms of energy evolution, velocity dispersions, angular momentum dependence, and stellar unbinding.

4.2.3 Perturber trajectory and disk encounter

Figure 9 shows the trajectory of the orthogonal perturber relative to the stellar disc. The perturber crosses the disc plane at $t \simeq 244.45$ Myr, producing a brief but impulsive gravitational interaction. Prior to the encounter, the disc remains thin and dynamically cold, while after the crossing it exhibits visible vertical disturbances and enhanced stellar scattering.

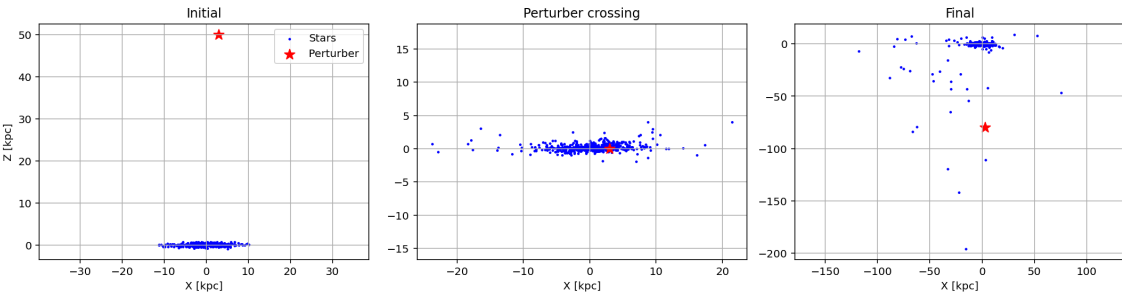


Figure 9: Orthogonal trajectory of the perturber.

4.2.4 Energy conservation and energy injection

Figure 10 demonstrates energy conservation throughout the simulation. The relative energy error remains small, confirming the numerical stability of the leapfrog integrator. A clear increase in total disk energy occurs at the time of perturber crossing, indicating physical energy injection rather than numerical artifacts.

During the encounter, the energy of the bound stellar population temporarily becomes more negative, reflecting the preferential removal of high-energy stars. Concurrently, a subset of stars gains positive energy and becomes unbound, carrying energy away from

the disk. After the encounter, the total energy settles at a less negative value, indicating permanent heating of the disk.

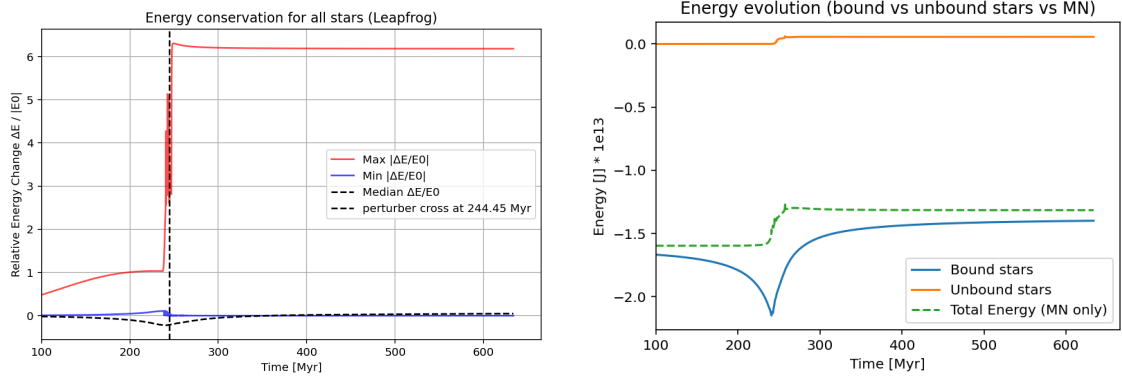


Figure 10: The left panel shows the energy conservation, while the right panel shows the physical energy injection and redistribution.

4.2.5 Energy change vs angular momentum

Furthermore, it has been observed that Stars with lower angular momentum experience larger fractional energy changes, indicating that inner disk stars are more strongly affected by the orthogonal perturber. This reflects the increased tidal susceptibility of stars on tighter orbits.

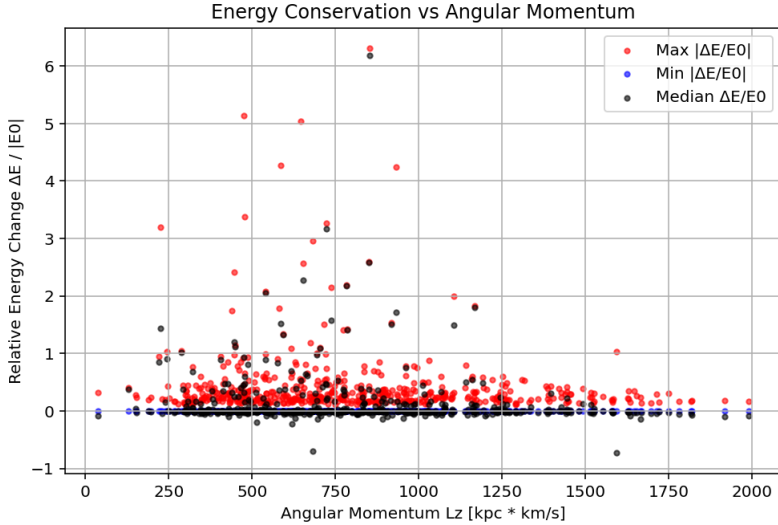


Figure 11: Relative energy change with respect to angular momentum.

4.2.6 Velocity dispersion evolution

It can be clearly demonstrated from Figure 12 that Both σ_R and σ_Z exhibit sharp increases, coincident with the perturber's disk crossing, followed by saturation at higher values. This demonstrates impulsive heating of the disk and a permanent increase in random stellar motions.

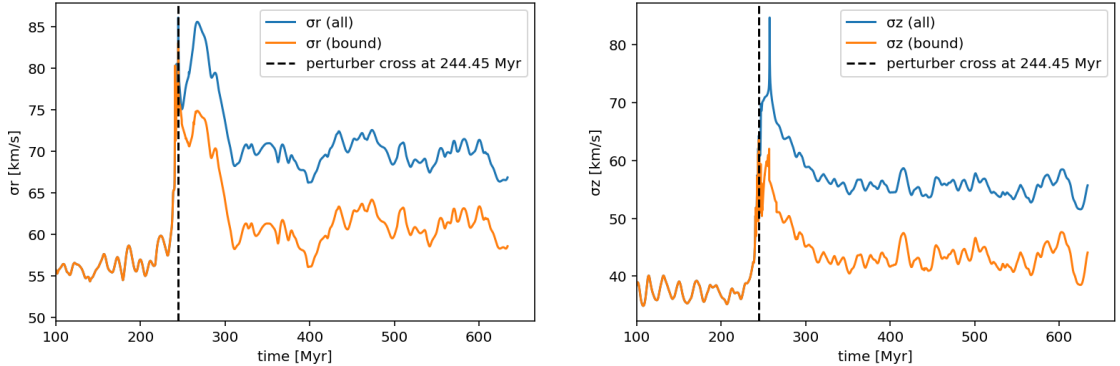


Figure 12: The left panels shows evolution of σ_R while the right shows the evolution of σ_Z .

4.2.7 Disk structure and unbound Stars

Moreover, from Figure 13 we can distinguishing between bound and unbound stars. It becomes evident that unbound stars are preferentially ejected to large vertical distances and exhibit coherent spatial structures, while the bound disk becomes thicker and dynamically heated. However, the right panel presents stellar unbinding occurring almost exclusively during the brief interval around the perturber crossing. After the encounter, the number of unbound stars remains constant, indicating that stripping is impulsive rather than continuous.

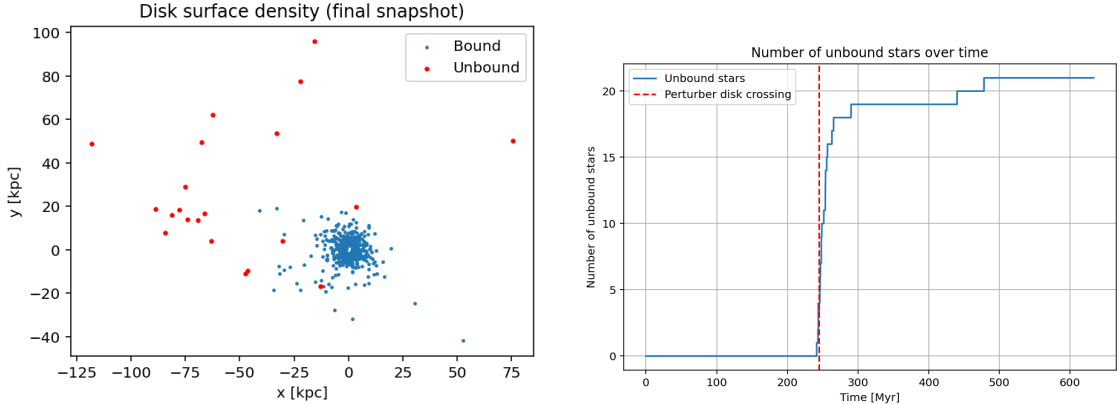


Figure 13: The left panels shows the structure of disk after perturbation while the right shows the number of stars ejected from the disk plane.

4.2.8 Conclusion

Overall, the orthogonal perturber produces strong impulsive heating, localized primarily near the impact radius. The encounter leads to vertical disk thickening, enhanced velocity dispersions, and the ejection of a small fraction of stars. These results are consistent with expectations for perpendicular tidal perturbations and provide a baseline for comparison with inclined encounters.

4.3 Inclined Perturber

4.3.1 Perturber trajectory and disk encounter

The perturber crosses the disk at an inclination of 30° , interacting with the disk over a longer path compared to the orthogonal case. As a result, the disk crossing occurs later, at $t = 288.26$ Myr, compared to $t = 244.45$ Myr for the orthogonal passage. During the encounter, stars are displaced both radially and vertically along the perturber's inclined trajectory, leading to asymmetric ejection. After the passage, the disk remains vertically thickened with a population of displaced and unbound stars, indicating sustained heating.

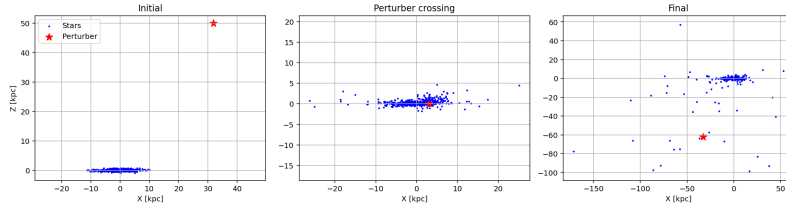


Figure 14: Trajectory of inclined perturber.

4.3.2 Energy change vs energy injection

The left panel shows the relative energy change, $\Delta E/E_0$, as a function of time for the inclined perturber case. The median and minimum values remain nearly constant throughout the evolution, indicating that the majority of disk stars experience only weak perturbations and that global energy conservation is well maintained. The maximum $\Delta E/E_0$ begins to rise gradually after ~ 100 Myr due to the approaching perturber and increases sharply at the disk crossing time, $t = 288.26$ Myr. After the encounter, the maximum value saturates at $\Delta E/E_0 \simeq 4.8$, which is lower than the orthogonal case. This reflects a more distributed energy injection during the inclined passage, where energetic stars are progressively heated and ejected rather than impulsively accelerated.

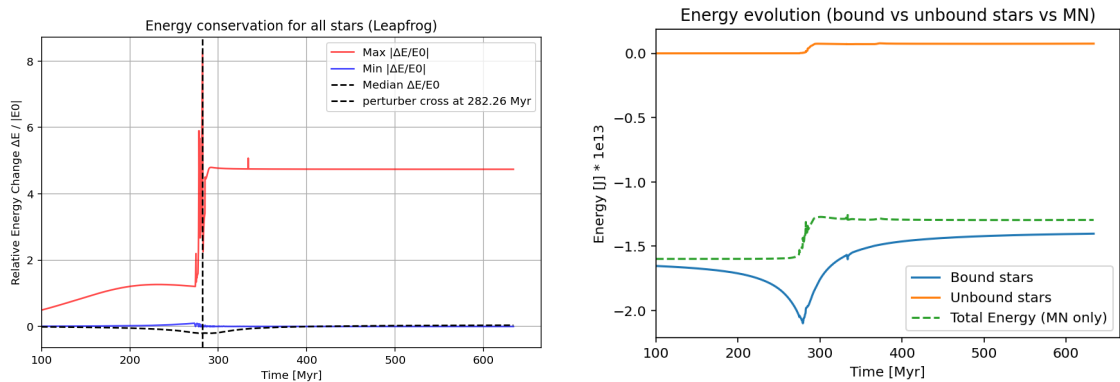


Figure 15: Energy change vs energy injection.

The right panel presents the relative energy change as a function of angular momentum, L_z . Stars with lower L_z exhibit larger energy variations, indicating that inner-disk stars are more strongly affected by the perturber. Higher- L_z stars remain largely unperturbed, preserving their initial orbital structure. Compared to the orthogonal encounter, the inclined case shows a reduced population of extreme high- $\Delta E/E_0$ outliers, consistent with smoother, long-duration coupling between the perturber and the disk.

4.3.3 Energy change vs angular momentum

In the inclined encounter, stars with low angular momentum again show the largest relative energy changes, confirming that the inner disk is most strongly affected. Compared to the orthogonal case, a small number of stars reach higher values, with $\Delta E/E_0$ up to ~ 8.2 , while a few others lie around ~ 6 . This indicates that the inclined passage can impart stronger energy kicks to a limited subset of stars due to prolonged interaction. The overall trend with L_z remains unchanged, with high- L_z stars largely unaffected.

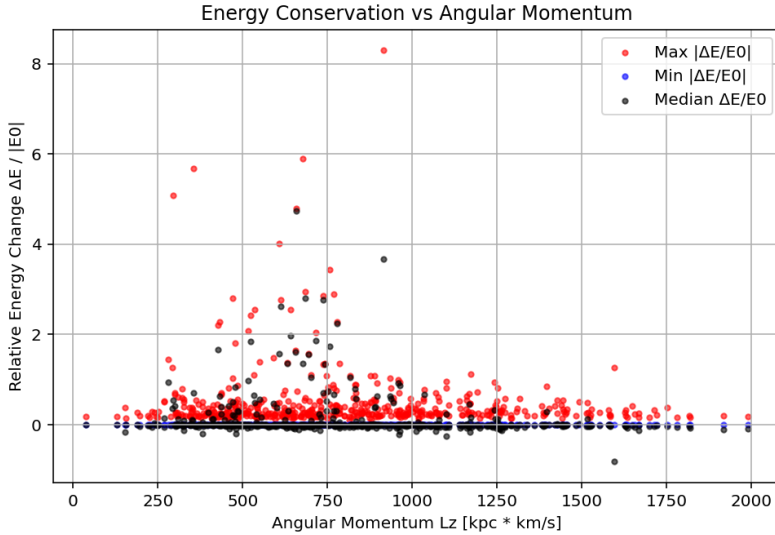


Figure 16: Energy change with respect to angular momentum.

4.3.4 Velocity dispersion evolution

At the crossing, both σ_R and σ_z rise sharply, reflecting strong heating of the stellar disk. In the inclined case, σ_R settles at a slightly higher value compared to the orthogonal case, while σ_z eventually reaches nearly the same level as in the orthogonal case. A secondary spike in σ_z around $t \sim 335$ Myr indicates continued vertical oscillations of stars after the main crossing, which likely dissipates excess vertical energy and explains why σ_z settles at a value comparable to the orthogonal encounter. Radially, stars near the impact radius ($R \sim 3$ kpc) show the largest increase in both dispersions, highlighting localized disk heating and vertical thickening along the perturber's path.

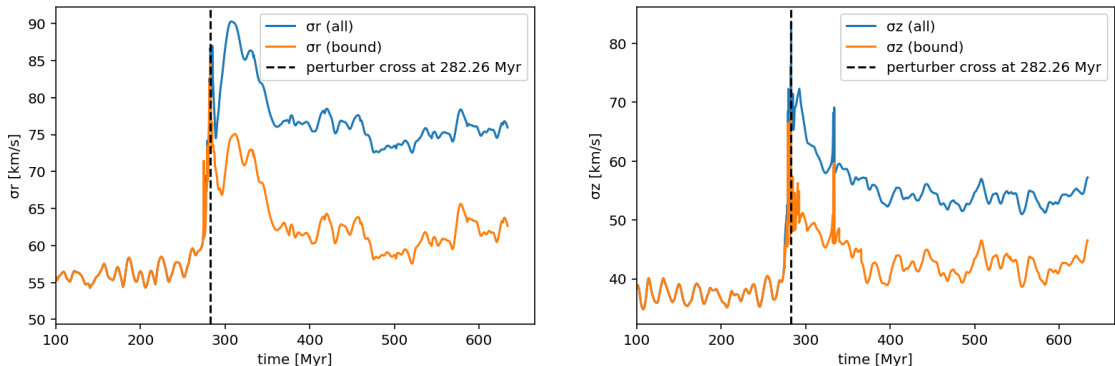


Figure 17: Evolution of velocity dispersion profiles.

4.3.5 Disk structure and unbound Stars

It is evident from Figure 18 that the bound disk becomes thicker and dynamically heated after perturbation. The number of unbound stars reaches up to 24, slightly higher than 21 in the orthogonal case, reflecting the longer interaction of the inclined trajectory. Stellar unbinding occurs almost exclusively around the disk crossing, after which the unbound population remains roughly constant, indicating impulsive stripping.

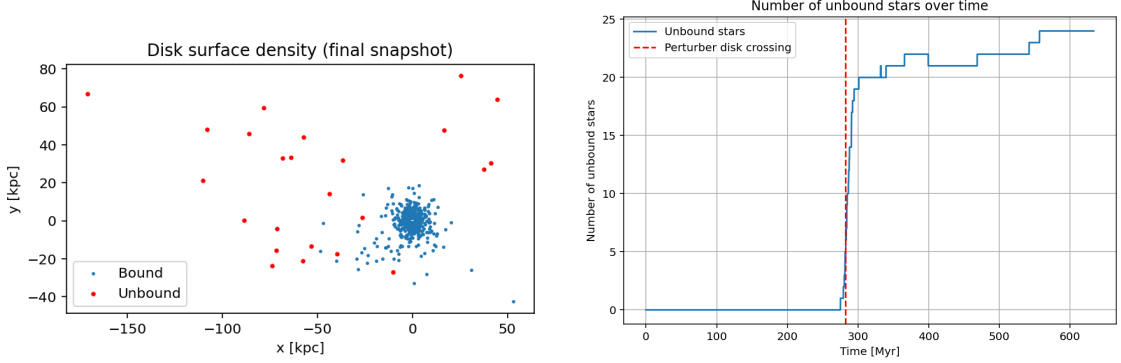


Figure 18: Disk structure and number of unboud stars.

4.3.6 Conclusion

In summary, the inclined perturber induces a longer, more gradual interaction with the disk compared to the orthogonal case. Disk stars experience significant vertical heating and localized thickening, while radial dispersions increase moderately. The maximum relative energy change and the number of unbound stars are slightly lower and higher, respectively, reflecting the prolonged energy transfer and gradual ejection of stars. Overall, the inclined passage produces smoother disk heating and a dynamically thickened, yet stable, stellar disk structure.

5 Perspectives on parallelization

The simulations presented in this project involve the integration of a large number of stellar orbits evolving in a fixed gravitational potential. In the collisionless approximation adopted here, and in the absence of self-gravity, the motion of each star is independent of the others. This independence makes the problem particularly well suited for parallel computation.

5.1 Parallelization strategy

Because the equations of motion are decoupled between stars, parallelization naturally applies to the stellar population rather than to the time integration. Individual stars, or groups of stars, can therefore be evolved simultaneously while sharing the same background potential and, when present, the same external perturbation. The time evolution itself must remain sequential, as each timestep depends on the state of the system at the previous one.

5.2 Possible implementations

In practice, the total set of N stars could be divided into several subsets, each evolved in parallel on a different processing unit within a shared-memory environment. This approach would require only minor modifications to the existing code, since the numerical schemes and equations of motion remain unchanged.

An alternative strategy would consist in parallelizing the numerical loops involved in the force evaluation and orbit integration. Given the vectorized formulation adopted in this work, such an approach could further reduce the computational cost while preserving code simplicity and readability.

For substantially larger simulations, a distributed-memory approach could also be envisaged, in which different computing units evolve distinct subsets of the stellar population. This would, however, require explicit data communication and synchronization between processes, and was therefore beyond the scope of the present project.

5.3 Benefits and limitations

Parallel execution would significantly reduce the wall-clock time of the simulations, enabling the exploration of larger stellar samples, longer integration times, or multiple perturbation scenarios. This would be particularly useful for convergence studies or parameter-space surveys.

However, the achievable performance gain would be limited by communication overheads and by inherently serial parts of the code, such as data input/output and post-processing. As a result, parallelization would be most effective for simulations with a large number of particles, where the cost of orbit integration dominates the total runtime.

Overall, although the present study relies on a serial implementation, its structure is well suited for parallel execution, and several straightforward strategies could be employed to extend it efficiently.

Conclusion

In this project, we implemented and tested numerical integration of stellar orbits in a Miyamoto–Nagai potential using the cylindrical Leapfrog method and Runga-Kutta 4. The results demonstrate excellent conservation of energy and angular momentum, confirming the stability and accuracy of the symplectic integrator with respect to Runga-Kutta-4. Radial and vertical velocity dispersions remain consistent with the initial conditions, validating the equilibrium setup. Limitations include the neglect of non-axisymmetric perturbations, self-gravity of the disk, and more realistic time-dependent potentials. Future work could incorporate a live disk with multiple interacting stars, and fly-by external perturbations to study dynamical heating and migration. Overall, the numerical framework provides a robust tool for studying disk dynamics in simplified galactic potentials.

GitHub link to access the codes: <https://github.com/Annus-ctrl/Galactic-Disk-Heating>

References

- [1] Nagai R. Miyamoto M. “Three-Dimensional Models for the Distribution of Mass in Galaxies”. In: *Astronomical Society of Japan* 27.4 (1975), pp. 533–543.
- [2] Tremaine S. Binney J. “Galactic Dynamics: Second Edition”. In: *Princeton: The University press* (2008).